IEEE Access
Multidisciplinary | Rapid Review | Open Access Journal

Received November 24, 2020, accepted December 9, 2020, date of publication December 17, 2020,
date of current version December 31, 2020.

Digital Object Identifier 10.1109/ACCESS.2020.3045390

Control System for a Single-Phase DC-Excited Flux-Switching Machine With a Torque Ripple Reduction Scheme

ZIH-CING YOU AND SHENG-MING YANG, (Member, IEEE)
Department of Electrical Engineering, National Taipei University of Technology, Taipei 10608, Taiwan
Corresponding author: Sheng-Ming Yang (smyang@ntut.edu.tw)

This work was supported by the Ministry of Science and Technology of Taiwan, R.O.C., under Grant MOST 107-2221-E-027-082-MY3.

ABSTRACT Single-phase dc-excited flux-switching machines (DCFSMs) are suitable for operations in harsh environments and cost-sensitive applications due to their rugged structure. However, the practical application of DCFSMs is limited because significant torque ripple is generated in them as the armature current commutates. However, with a marginal modification to the rotor structure, the single-phase DCFSM exhibits a unique property that its reluctance torque is complementary to its electromagnetic torque. A significant reluctance torque can be generated by the field current near the commutation positions. To explore the characteristics of the complementary torque, this paper presents a speed control system with a torque ripple reduction scheme for single-phase DCFSMs. In this scheme, the armature and field currents are controlled with precalculated profiles such that the reluctance torque compensates for the loss of the electromagnetic torque near the commutation positions. The experimental results indicated that with the proposed control scheme, the maximum torque ripple reduced to 56% near the commutation positions when the machine provided the rated torque. Moreover, because the studied DCFSM generated highly linear torque, satisfactory speed control performance was achieved.

INDEX TERMS Control system, reluctance torque, single-phase flux-switching machine, torque ripple reduction.

I. INTRODUCTION

Because single-phase dc-excited flux-switching machines (DCFSMs) contain only windings and iron cores, their manufacturing cost is low. Moreover, DCFSMs are suitable for operation in harsh environments and for high-speed operations due to their rugged structure [1]–[3]. Numerous studies have reported that single-phase DCFSMs exhibit higher efficiency and power density than single-phase induction machines (IMs) and universal machines (UMs) [4]–[7]. Therefore, single-phase DCFSMs have the potential to be used in the applications in which single-phase IMs or UMs are adopted, such as low power food processor, juicer, and mixer.

Single-phase DCFSMs contain two types of windings: armature and field windings. Conventionally, the armature current commutates with mutual inductance, whereas the field current is set to a dc value. However, significant torque ripple is also generated due to armature current commutation. When the armature current commutates, the electromagnetic torque reduces to 0. Consequently, the torque ripple is generally more than 100% of the rated torque. In addition, single-phase DCFSMs cannot generate sufficient starting torque near the commutation positions at standstill. The commutation position denotes the position where the armature current commutates. The aforementioned drawbacks limit the application of DCFSMs. To provide single-phase machines with self-starting capability, the authors in [8]–[12] presented techniques that used tapered rotor design and a special magnet arrangement. By adopting these techniques, the rotor can be moved to a nonzero-torque position by cogging torque at standstill. Consequently, the single-phase machines can successfully start-up. However, additional cost and installation space is required for the permanent magnets. In [3], a prototype machine with a two-layer rotor structure was proposed. With this rotor structure, the field current can generate significant reluctance torque near the commutation positions. It is called the complementary torque characteristic in this

The associate editor coordinating the review of this manuscript and approving it for publication was Atif Iqbal.

paper. Because the rotor can be moved to a nonzero-torque position by the reluctance torque, this prototype machine can start-up from any rotor position. However, the control scheme for reducing the torque ripple was not discussed in [3]. Torque ripple reduction scheme for three-phase machines have been discussed extensively in the literatures. These schemes are generally based on the predictive control [13]–[16], and current shaping techniques [17]–[19]. Reference [20] presented the design of a unique current profile to reduce torque ripple on the basis of current shaping technique for single-phase DCFSM; however, only preliminary results are presented in this study.

In this paper, a torque ripple reduction scheme is presented for the prototype machine constructed in [3]. Due to the two-layer rotor structure, this machine has a unique property that its reluctance torque is complementary to its electromagnetic torque. Significant reluctance torque can be generated by the field current near the commutation positions. The proposed torque ripple reduction scheme was developed according to the complementary torque. The machine was excited with the calculated armature and field current profiles so that the reluctance torque could compensate for the pulsating electromagnetic torque.

The remainder of this paper is organized into five sections. Section II describes the structure and model of the studied machine. Section III presents the algorithms for the current profile calculations. Section IV describes the current and speed control systems. Section V describes the performance of the proposed control system. Finally, Section VI provides the conclusions of this study.

II. STUDIED SINGLE-PHASE DCFSM

The machine studied in this research is an eight-slot, four-pole, single-phase DCFSM (Fig. 1(a)). Its rotor is composed of a main rotor, which has a standard doubly salient structure, and an auxiliary rotor, which has an asymmetric pole shoe structure [3]. Its cross-sectional view is displayed in Fig. 1(b) to show the winding configuration, where θ_r is the rotor electrical position. For a clear observation, only the main rotor is shown. The main parameters of the machine are listed in Table 1, where the active material weight denotes the total weight of the iron cores and copper windings.

The torque generated by the single-phase DCFSM can generally be expressed as follows:

$$T_e = P\left[\frac{i_a^2}{2}\frac{d}{d\theta_r}L_{as} + \frac{i_f^2}{2}\frac{d}{d\theta_r}L_{fs} + i_a\frac{d}{d\theta_r}\left(i_f L_m\right)\right] = T_{relucA} + T_{relucF} + T_m, \quad (1)$$

where P is the number of poles; i_a and i_f are the armature and field currents, respectively; L_{as} and L_{fs} are the armature and field self-inductances, respectively; and L_m is the mutual inductance. The generated torque comprises three components: (i) the electromagnetic torque generated by both currents and the mutual inductance (T_m), (ii) the reluctance torque generated by the armature current and its self-inductance (T_{relucA}), and (iii) the reluctance torque generated by the field current and its self-inductance (T_{relucF}). Fig. 2 displays the self-inductances and mutual inductance calculated with the finite-element method (FEM). The inductances fluctuate with the rotor position. Fig. 3(a) displays the calculated T_m and the currents when the machine is excited using the conventional method, in which the armature current is sinusoidal and the field current has a constant value. Due to the armature current commutation, T_m pulsates considerably. However, as displayed in Fig. 3(b), when the currents are constant, a nearly square T_{relucF} is generated near the commutation positions. Because the reluctance torque is highly complementary to the electromagnetic torque, the reluctance torque can compensate for the loss in the electromagnetic torque caused by the armature current commutations. Although the reluctance torque will counteract the electromagnetic torque when the armature current is significant, the influence is negligible due to significant electromagnetic torque.

TABLE 1. Main parameters of the single-phase DCFSM.

Parameters	Value	Unit
Stator outer radius	50	mm
Stack length	30	mm
Rated voltage	150	V
Rated speed	3500	rpm
Maximum speed	6000	rpm
Rated torque	0.64	N-m
Active material weight	1.649	Kg

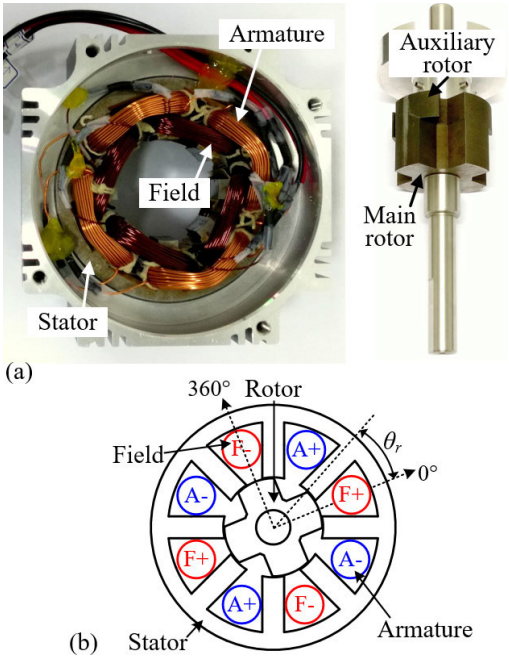

FIGURE 1. (a) Image of the studied single-phase DCFSM, and (b) its cross-sectional view (only main rotor).

III. CURRENT PROFILES FOR REDUCING THE TORQUE RIPPLE

The torque components displayed in Fig. 3 reveal that increasing the field current near the commutation positions can

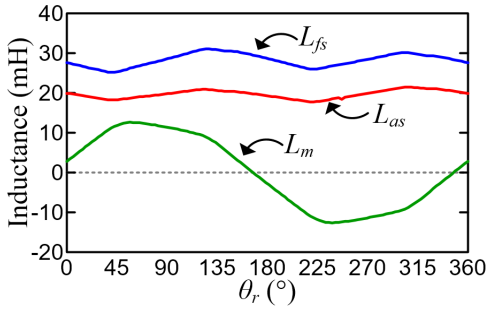

FIGURE 2. Calculated self-inductances and mutual inductance.

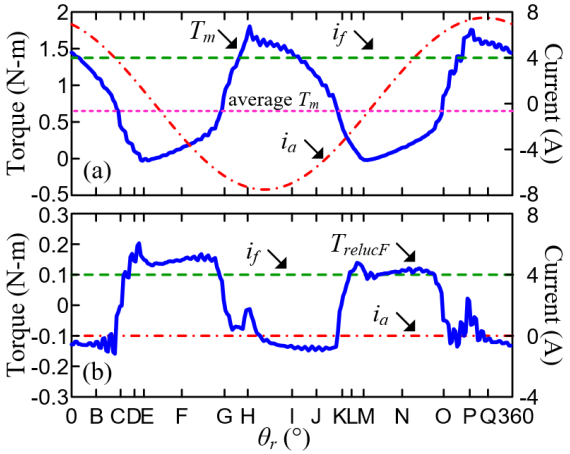

FIGURE 3. Calculated (a) T_m and (b) T_{relucF} with the respective excitation currents.

reduce the torque ripple. However, simply increasing the field current without regulating the armature current suitably may cause excessive copper loss. Moreover, the input power supply also limits the maximum rate of change of the currents. The aforementioned constraints were considered in the development of a current profile calculation algorithm.

A. CURRENT PROFILES WITH MINIMUM COPPER LOSS

Because the currents are controlled independently, an infinite number of current combinations can generate a desired torque. An algorithm was developed in [8] to calculate the current profiles for various torque commands and minimize the copper loss. Fig. 4 displays a set of calculated current profiles, where T_{e0}, T_{e1}, T_{e2}, T_{e3}, and T_{e4} denote 0%, 25%, 50%, 75%, and 100% rated torque, respectively. According to the results of [8], the maximum torque ripple reduced considerably to 30% with the aforementioned profiles, in which the torque ripple is calculated as follows: $[\max(T_e) - \min(T_e)]/\text{mean}(T_e)$. However, these aforementioned profiles are impractical for implementation because the sharp transitions near the commutation positions cannot be realized with a real input power supply. Consequently, the generated torque deteriorates at high speed when the studied machine is excited with the aforementioned current profiles.

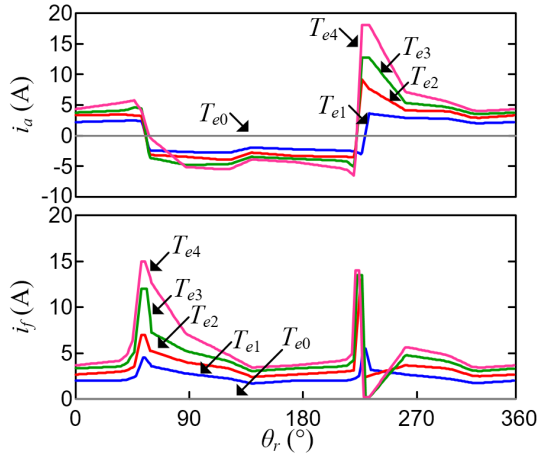

FIGURE 4. Calculated current profiles for various torque commands to reduce the torque ripple and minimize the copper loss [8].

B. CURRENT PROFILES THAT CONSIDER THE INPUT VOLTAGE LIMITATION

To maintain the torque performance at high speed, the rate of change of the currents should be limited according to the input voltage limitation. The armature winding voltage v_a and field winding voltage v_f can respectively be expressed as

$$v_a = i_a R_a + \omega_r \frac{d}{d\theta_r}(i_a L_{as}) + \omega_r \frac{d}{d\theta_r}(i_f L_m), \tag{2}$$

$$v_f = i_f R_f + \omega_r \frac{d}{d\theta_r}(i_f L_{fs}) + \omega_r \frac{d}{d\theta_r}(i_a L_m), \tag{3}$$

where R_a and R_f are the resistances of the armature and field windings, respectively, and ω_r is the electrical speed. Coupling voltages are formed between the windings due to the mutual inductance. The induced voltage on the armature winding is treated as the back electromotive force (EMF). The resistive drop is neglected because this factor is considerably smaller than the inductive drop and induced voltage at high speed. Thus, the differential voltage caused by the current variations can be approximated as follows:

$$\frac{d}{d\theta_r}(i_a L_{as}) \approx \frac{1}{\omega_r}\left(v_a - \omega_r \frac{d}{d\theta_r}(i_f L_m)\right) \tag{4}$$

$$\frac{d}{d\theta_r}(i_f L_{fs}) \approx \frac{1}{\omega_r} \cdot \left(v_f - \omega_r \frac{d}{d\theta_r}(i_a L_m)\right) \tag{5}$$

According to (4) and (5), the winding voltage and induced voltage determine the rate of change of the current. Near the commutation positions, the induced voltage in the field winding is small due to a small i_a. Therefore, v_f is generally sufficient for obtaining a suitable rate of change for the field current. However, for the armature winding, the back EMF becomes significant near the commutation positions due to the increasing field current. Therefore, the rate of change of the armature current is limited to the available v_a.

In this study, the currents were controlled separately by using two full-bridge inverters. The maximum voltage that can be applied to the windings is equal to the input power supply V_{DC}. Therefore, the rate of change of the armature

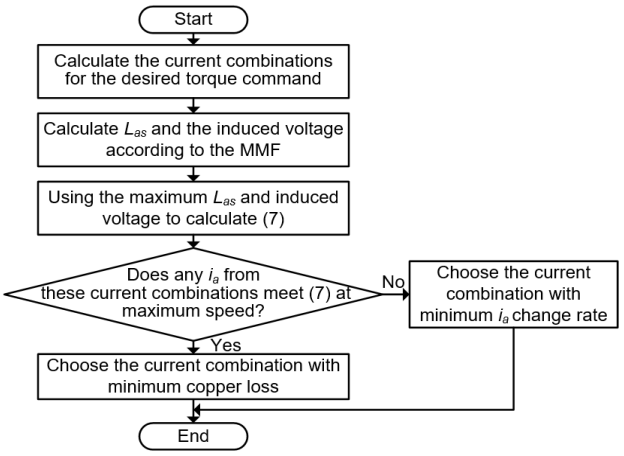

FIGURE 5. Flow of the proposed current profile design algorithm.

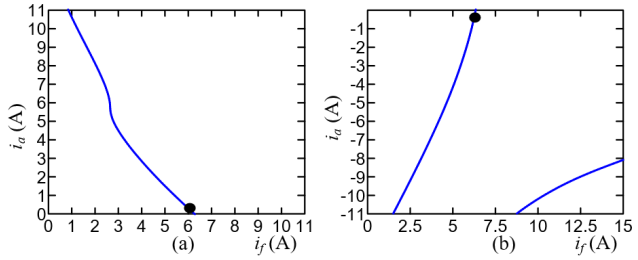

FIGURE 6. Current combinations that can generate 50% rated torque for positions (a) D and (b) E.

current must satisfy the following inequality:

$$\left|\frac{d\left(i_a L_{as}\right)}{d\theta_r}\right| \leq \frac{1}{\omega_r}\left(|\pm V_{DC}| - |\text{backEMF}|\right). \tag{6}$$

Absolute values are used in (6) to avoid the error caused by the polarity. Equation (6) can also be expressed as

$$\left|\frac{\Delta\left(i_a L_{as}\right)}{\Delta\theta_r}\right| \leq \frac{1}{\omega_r}\left(|\pm V_{DC}| - |\text{backEMF}|\right), \tag{7}$$

where "Δ" denotes the difference. A current profile calculation algorithm was developed on the basis of (7) and the inductance model displayed in Fig. 2. The flow of the algorithm is illustrated in Fig. 5.

The principle of the proposed algorithm is described in the following text, consider the positions D and E marked in Fig. 3. Assuming that the torque command is 50% rated torque, the current combinations that can generate 50% rated torque are calculated and shown in Fig. 6. Then, because L_{as} and the back EMF are considerably affected by the excitation current, they are calculated according to the magnetomotive force (MMF) produced by these current combinations. The MMF is calculated as follows:

$$\text{MMF} = i_a N_a + i_f N_f, \tag{8}$$

where N_a and N_f denote the number of turns of the armature and field windings, respectively. The calculated L_{as} values and back EMFs for the aforementioned current combinations

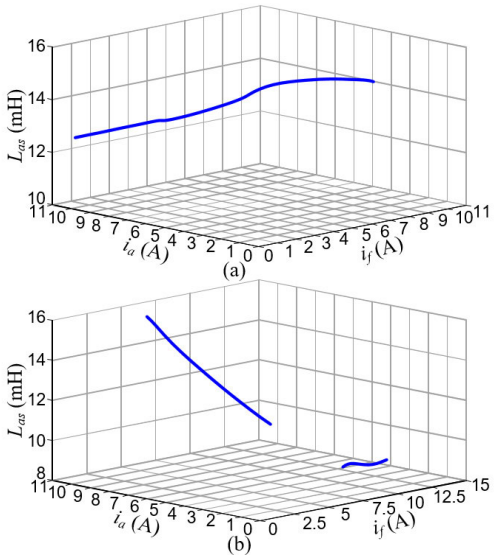

FIGURE 7. Calculated L_{as} for the current combinations displayed in Fig. 6: positions (a) D and (b) E.

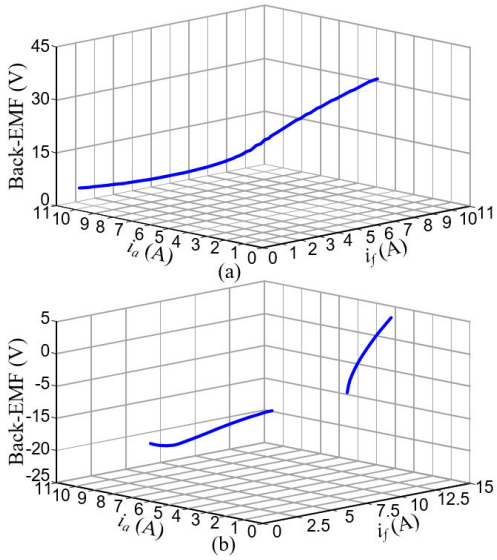

FIGURE 8. Calculated induced voltage for the current combinations displayed in Fig. 6: positions (a) D and (b) E.

are displayed in Figs. 7 and 8, respectively. The largest L_{as} and back EMF values are used in (9) to calculate the worst case, expressed as

$$\max\left(L_{as}\right)\left|\frac{\Delta i_a}{\theta_E - \theta_D}\right| \leq \frac{1}{\omega_r}\left(V_{DC} - \max\left(|\text{backEMF}|\right)\right). \tag{9}$$

After the rate of change of the armature current is calculated, the current combinations that satisfy (9) at the maximum speed will be saved. Then, the copper loss of these current combinations are calculated by (10).

$$P_{copper} = i_a^2 R_a + i_f^2 R_f. \tag{10}$$

Finally, the current combination that generates minimum copper loss is selected and used in the torque ripple reduction

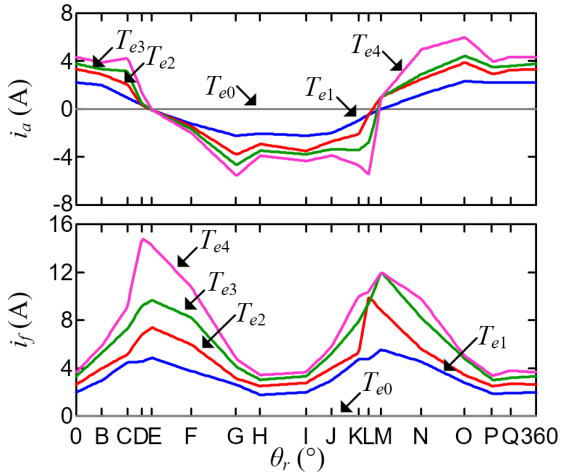

FIGURE 9. Current profiles calculated with the proposed algorithm.

scheme. The selected current combination is marked in Fig. 6 with a black dot. When no current combination satisfies (9), the current combination with the minimum armature current change rate is selected.

C. PROPOSED CURRENT PROFILES

Fig. 9 depicts the current profiles for various torque commands obtained with the proposed calculation algorithm. The armature current becomes smoother after its change rate is limited. The field current profile also becomes smoother due to the slow commutation in the armature winding. Only the positions marked in Fig. 3 (0°, B–Q, and 360°) are calculated to save computation time. The currents between these positions are approximated through linear interpolation.

IV. CONTROL SYSTEMS

The control scheme for single-phase DCFSM has been rarely discussed. Some studies have proposed controlling single-phase brushless dc motors [21] and single-phase IMs [22]–[24] on the basis of the virtual DQ frame orientation. The results of these studies have indicated that single-phase machines can be controlled in a similar manner to three-phase machines. However, the schemes used to control three-phase machines cannot be implemented in single-phase DCFSMs because the magnetic field distribution of DCFSMs is not sinusoidal.

Fig. 10 displays the proposed control scheme for the studies single-phase DCFSM. The control system consists of three parts: the (i) current controller, (ii) current command generator, and (iii) speed controller. An encoder is used to feedback the rotor position and shaft speed to validate the performance of the proposed scheme. The subsequent sections detail on the three aforementioned controllers.

A. CURRENT CONTROLLER

Equations (2) and (3) can be rewritten respectively as

$$v_a = i_a R_a + L_{1a}\frac{d}{dt}i_a + \omega_r \frac{d\,(i_a L_{2a})}{d\theta_r} + \omega_r \frac{d\,(i_f L_m)}{d\theta_r} \qquad (11)$$

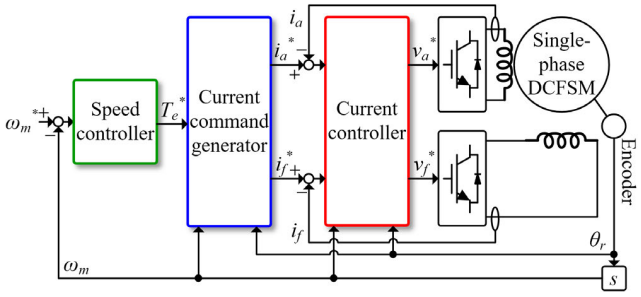

FIGURE 10. Control system for the studied single-phase DCFSM.

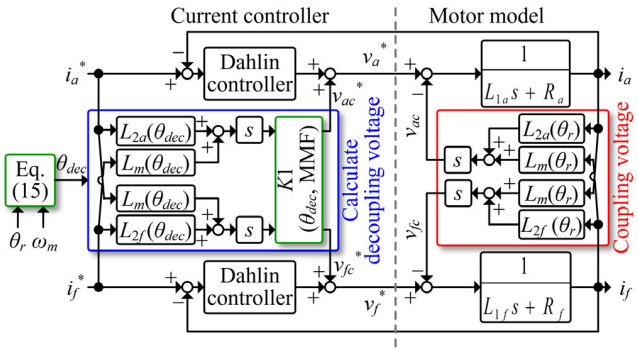

FIGURE 11. Function blocks of the current controller.

and

$$v_f = i_f R_f + L_{1f}\frac{d}{dt}i_f + \omega_r \frac{d\,(i_f L_{2f})}{d\theta_r} + \omega_r \frac{d\,(i_a L_m)}{d\theta_r}, \qquad (12)$$

where L_{1a} and L_{1f} are the dc components of the armature and field self-inductances, respectively. Moreover, L_{2a} and L_{2f} are the ac components of the armature and field self-inductances, respectively. Fig. 11 displays the detailed function blocks of the current controller. The windings are modeled as R–L loads with coupling voltages between them, which are expressed as follows:

$$v_{ac} = \omega_r \cdot \frac{d}{d\theta_r}(i_a L_{2a}) + \omega_r \cdot \frac{d}{d\theta_r}(i_f L_m) \qquad (13)$$

$$v_{fc} = \omega_r \cdot \frac{d}{d\theta_r}(i_f L_{2f}) + \omega_r \cdot \frac{d}{d\theta_r}(i_a L_m) \qquad (14)$$

All the coupling voltages are functions of the rotor position due to the alternating inductances and are decoupled with v_{ac}^* and v_{fc}^* in the controller, as depicted in the blue block in Fig. 11. The inductances used to calculate the decoupling voltages are displayed in Fig. 2. The currents are controlled with the Dahlin controller because it can achieve considerably high bandwidth without overshoot [25]. The controller bandwidth is approximately 1.6 kHz. Two full-bridge inverters are used to generate the requested voltages through pulse-width modulation (PWM). Note that using two inverters is not appropriate for small size, low-cost drives. But it can maximize the performance and provide high flexibility for control algorithm development. Considering practical implementation, a half-bridge circuit can be used for the field winding

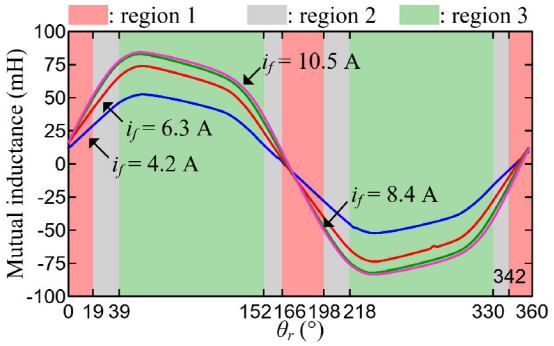

FIGURE 12. Calculated mutual inductances for various field currents.

since field current does not commutate. Consequently, a standard three-phase inverter module can be used to control both winding currents.

The inductances are stored in look-up tables (LUTs) and indexed with θ_{dec}. Because the voltage commands are synthesized through PWM with a digital signal processor (DSP), delays occur between the voltage commands and the actual voltages. Therefore, to apply the decoupling voltages promptly, the phase of θ_{dec} is set to be marginally ahead of that of θ_r. The parameter θ_{dec} is calculated as

$$\theta_{dec} = \theta_r + n \cdot T_s \cdot P\omega_m, \tag{15}$$

where T_s denotes the sampling period, and n is a positive integer. The parameter n is experimentally tuned to 2 to achieve the optimal compensation performance.

Another problem associated with the current controller is the inductance variations caused by magnetic saturation when the machine is subjected to heavy load. Rather than storing the inductances for different current levels, a gain $K1$ is introduced to compensate for the aforementioned variations and to simplify the control algorithm. To determine $K1$, the mutual inductance for various field currents is calculated, as displayed in Fig. 12. The fluctuation level of L_m is strongly dependent on the current. The variations in L_m are separated into three regions for the easy determination of $K1$. In region 1, the slope of L_m increases until i_f is near 8.4 A. Similarly, in region 2, the slope of L_m increases until i_f is nearly 6.3 A. However, in region 3, the slope of L_m is nearly constant. The aforementioned observations reveal that the saturation level varies with the rotor position and excitation current. Consequently, $K1$ is experimentally tuned for different position regions to compensate for the saturation-induced error. The $K1$ is also applied to L_{as} and L_{fs} because they share similar magnetic circuits. The magnitude of mutual inductance is different at various excitation current because of the nonlinear permeability of the iron core.

Fig. 13 depicts the setting of $K1$ for various MMF values. The parameter $K1$ reduces linearly from 0.95 to 0.5 in region 1 and from 0.95 to 0.38 in region 2. In region 3, $K1$ reduces linearly from 0.8 to 0.2. Because small discrepancies exist between the FEM model and the studied machine, $K1$ is not set to 1 even at low MMF values.

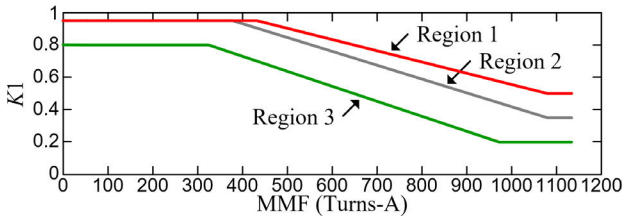

FIGURE 13. Plots of K1 versus MMF for various position regions.

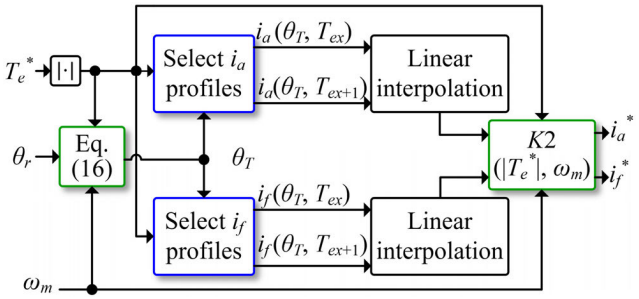

FIGURE 14. Function block of the current command generator.

B. CURRENT COMMAND GENERATOR

Fig. 14 displays the detailed function block of the current command generator. The armature and field current profiles in Fig. 9 are stored in LUTs. These LUTs have two inputs: the angle θ_T and the absolute value of the torque command $|T_e^*|$. Each LUT only stores five current waveforms that correspond to T_{e0}, T_{e1}, T_{e2}, T_{e3}, and T_{e4}. When $|T_e^*|$ is not equal to these values, two adjacent current waveforms are involved in the calculations. For example, when $|T_e^*|$ is 0.4 Nm, the current waveforms for T_{e2} and T_{e3} are used to calculate the current commands through linear interpolation. The table index θ_T is calculated as

$$\theta_T = \theta_r + m \cdot T_s \cdot P\omega_m, \tag{16}$$

where m is a positive integer. Similar to θ_{dec} in (15), the phase of θ_T is set to be marginally ahead of that of θ_r to compensate for the phase delay between the current command and the actual motor current. Because the current command contains ac components, the phase delay of the feedback current increases with speed due to the limited bandwidth of the controller. If the phase delay is not compensated, it negatively affects the torque performance at high speeds. To compensate for the phase delay appropriately, m is tuned experimentally according to the motor speed and torque command. Fig. 15 depicts the waveforms of m versus the speed for various torque commands. The parameter ω_m is the mechanical speed of the motor.

In addition to the phase error, a magnitude error occurs with the current controller as speed increases. The magnitude error deteriorates the torque performance. Another gain $K2$ is introduced to compensate for the torque loss caused by the magnitude error. Fig. 16 illustrates the waveforms of $K2$ versus the speed for various torque commands. These waveforms were also determined experimentally. The compensation increases with the speed and torque command. However,

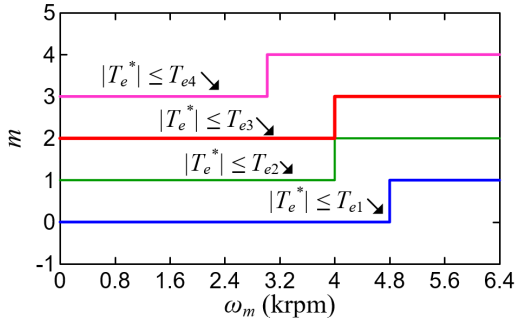

FIGURE 15. Waveforms of m versus speed for T_{e1}, T_{e2}, T_{e3}, and T_{e4}.

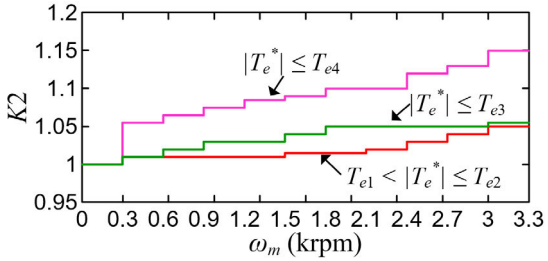

FIGURE 16. Waveforms of K2 versus speed for T_{e1}, T_{e2}, T_{e3}, and T_{e4}.

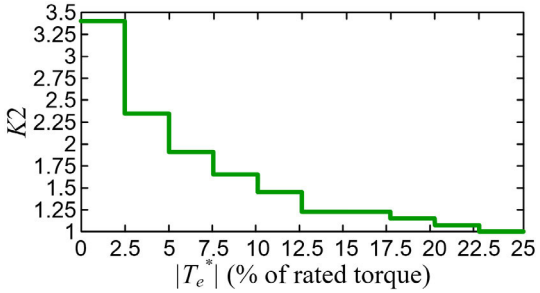

FIGURE 17. Waveform of K2 versus torque command for $|T_e^*| < T_{e1}$ (light load).

because the magnitude error caused by the core loss becomes significant at light loads, $K2$ must be adjusted according to $|T_e^*|$ and not the speed. Consequently, when $|T_e^*| < T_{e1}$, $K2$ is determined according to the waveform displayed in Fig. 17.

C. NEGATIVE TORQUE COMMAND

For negative torque command, the armature current waveform is reversed. However, the field current can only generate positive reluctance torque near the commutation positions. Therefore, to avoid disturbing the positive torque generation algorithm, the field current is set as 2, 2.8, 3.3, and 3.8 A for $|T_e^*| = T_{e1}$, $|T_e^*| = T_{e2}$, $|T_e^*| = T_{e3}$, and $|T_e^*| = T_{e4}$, respectively, when the torque command is negative. The aforementioned values are the minimum values of the i_f waveforms displayed in Fig. 9.

D. SPEED CONTROLLER

Fig. 18 illustrates the function block of the speed controller. The shaft speed is controlled with a proportional–integral controller. The parameter k_p is the proportional gain, and

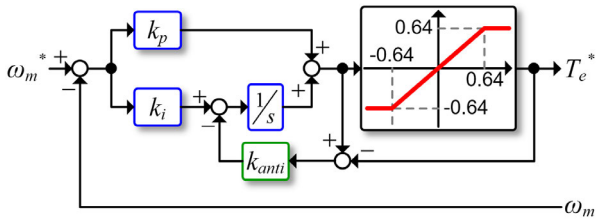

FIGURE 18. Function block of the speed controller.

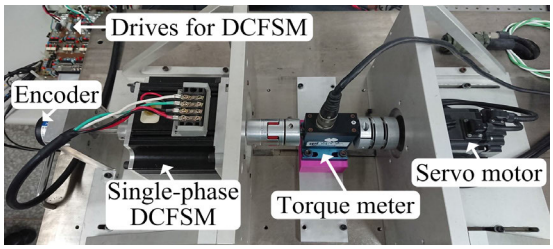

FIGURE 19. Experimental setup.

k_i is the integral gain. The bandwidth of the controller is tuned to 5 Hz. The torque command is limited to the rated value of ±0.64 Nm. Antiwindup control is implemented with a gain K_{anti} to avoid integral windup.

V. EXPERIMENTAL RESULTS

Fig. 19 illustrates the experimental setup. The studied single-phase DCFSM was coupled to a servo motor so that it could operate in the torque or speed mode. In the torque mode, the shaft speed was regulated by the servo motor and the DCFSM provided the load torque. By contrast, in the speed mode, the shaft speed was regulated by the DCFSM and the servo motor provided the load torque. An encoder with a resolution of 2000 pulses/revolution was used to feedback the rotor position and speed. A torque meter was connected between two motors to measure the shaft torque. The input dc voltage was 155 V. The proposed control scheme was implemented on a TMS320F28335 DSP. The sampling period of the current controller and current command generator was 62.5 μs. Moreover, the sampling period of the speed controller was 0.5 ms.

A. STEADY-STATE PERFORMANCE

Fig. 20 displays the torque response of the DCFSM at 60 rpm when the machine was excited with the proposed current profiles. The measured torque was consistent with the position for the 25% and 50% torque commands, the torque ripple was less than 20% at all the tested positions. However, for the 75% and 100% torque commands, significant decreases in torque were observed between the L and M positions. These positions correspond to the second commutation position of the machine. The maximum torque ripple increased to 32% and 56% at the L and M positions, respectively. Because the auxiliary rotor was easily saturated near the second commutation position, the saturated auxiliary rotor limited the reluctance

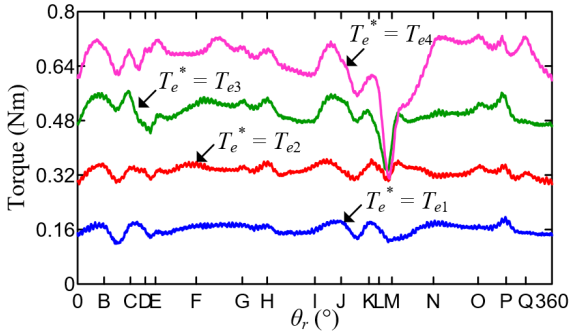

FIGURE 20. Measured torque versus position when the DCFSM was running at 60 rpm and excited with the proposed current profiles.

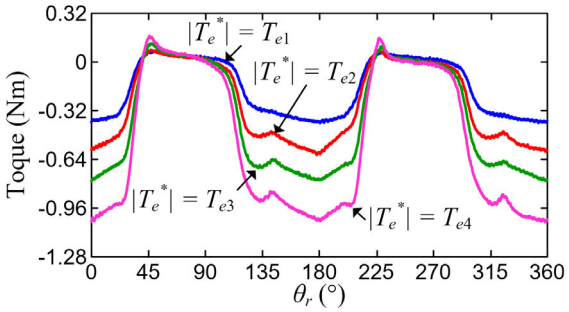

FIGURE 21. Measured torque versus position when the DCFSM was running at 60 rpm and excited with negative torque commands.

torque to approximately 0.32 Nm. Therefore, large torque reduction was observed. In addition, these results indicate that the studied machine has self-starting capability at any rotor position.

Fig. 21 displays the measured torque response for various negative torque commands. Torque pulsation inevitably appeared because the machine could not generate negative reluctance torque effectively, as explained in Section IV part C.

Fig. 22 presents a comparison of the torque performance achieved with the proposed current profiles and the primitive current profiles displayed in Fig. 4. The machine was operated in the torque mode with the 25% and 50% torque commands. The results were normalized with the rated torque (pu) for clear observation. The torque generated with the current profiles displayed in Fig. 4 reduced significantly as the speed increased due to the loss of torque at the commutation positions. The torque performance was more consistent with the proposed current profiles because the voltage limitation was included in the current profile calculations.

The torque–speed (T–N) curves of the DCFSM are displayed in Fig. 23. The solid lines and gray dots represent the results measured in the torque and speed modes, respectively. With the proposed control scheme, the machine could provide a constant rated torque within the rated speed (3500 rpm). For speeds higher than the rated speed, the torque decreased as the speed increased due to the power supply limitation. At the maximum speed (6000 rpm), the machine could still provide 50% rated torque.

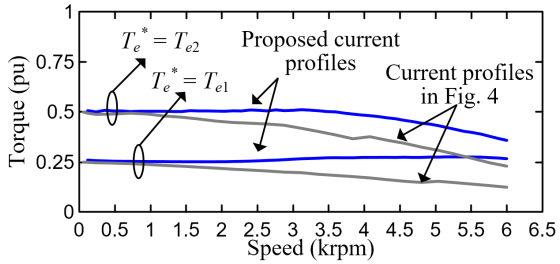

FIGURE 22. Comparison of the torque performance achieved with the proposed current profiles and the current profiles displayed in Fig. 4.

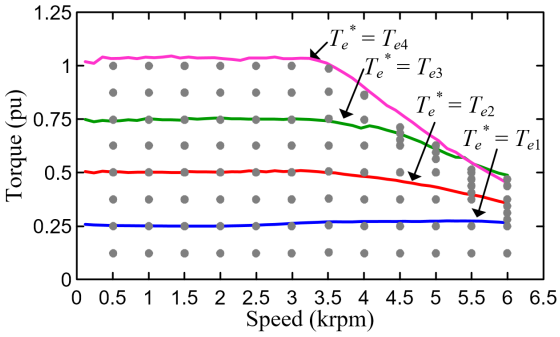

FIGURE 23. T–N curves measured in the torque and speed modes. The measured torque is normalized to the rated torque.

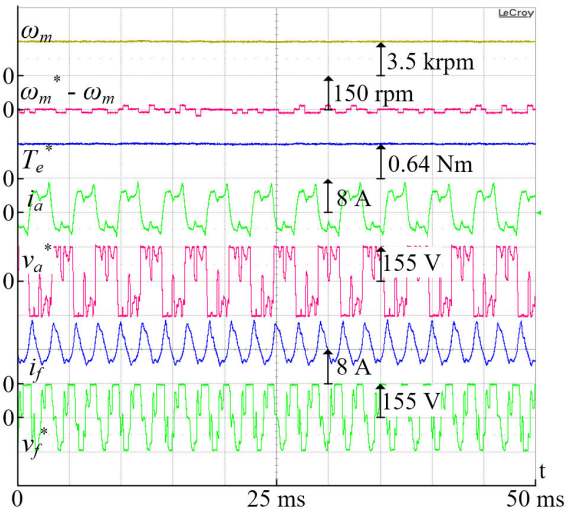

FIGURE 24. Steady-state responses of the control signals when the machine was running at 3500 rpm with 100% load.

Figs. 24 and 25 display the steady-state responses of various control signals when the machine was running at 3500 rpm with 100% load and at 6000 rpm with 50% load, respectively. The DCFSM was operated in the speed mode. Fig. 24 indicates that the winding voltages were marginally saturated with the dc power supply near the commutation positions. Consequently, the machine could not produce the rated torque above 3500 rpm. Moreover, as depicted in Fig. 25, the winding voltages were seriously saturated at 6000 rpm with 50% load. This result is in agreement with the extreme operating point in the T–N curve illustrated in Fig. 23. The aforementioned results validate that the studied

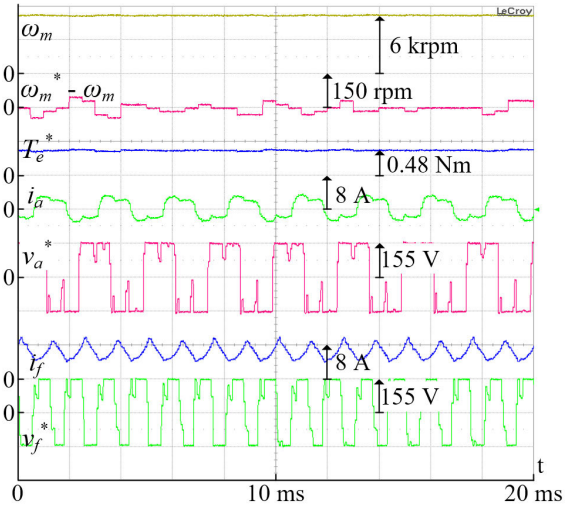

FIGURE 25. Steady-state responses of the control signals when the machine was running at 6000 rpm with 50% load.

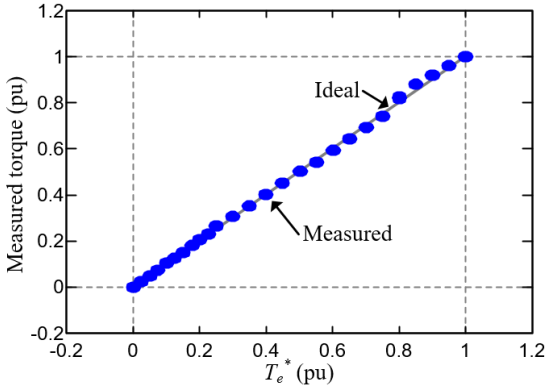

FIGURE 26. Measured average torque versus torque command at the rated speed. Both torques are normalized to the rated torque.

machine can run stably at the rated and maximum speeds with the maximum torque available at these speeds.

Fig. 26 illustrates the average torque measured at the rated speed for the various torque commands. The measured torque highly agreed with the torque command. This result validates that the studied machine can generate highly linear torque with the proposed control scheme.

B. DYNAMIC PERFORMANCE

The experimental results illustrated in Figs. 27–32 were obtained when the DCFSM was operated in the speed mode. Fig. 27 displays the responses when the machine accelerated from standstill to 3500 rpm within 1 s under 75% load. The motor speed tracked the speed command well, and the maximum speed error was approximately 200 rpm. The high-frequency oscillations associated with the speed error and T_e^* waveforms are caused by the mechanical vibration of the coupling between the encoder and the motor. Fig. 28 depicts the responses when the machine accelerated from standstill to 6000 rpm within 1.25 s under 35% load. Above 3500 rpm, the torque command increased because the torque

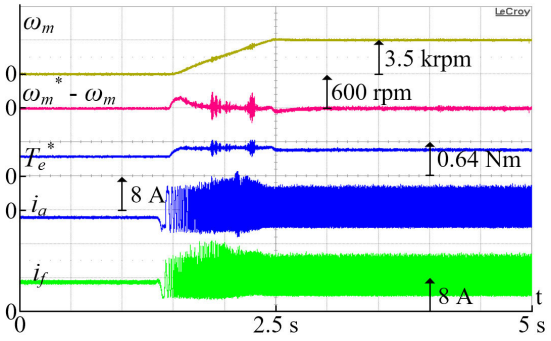

FIGURE 27. Responses when the machine accelerated from standstill to 3500 rpm within 1 s under 75% load.

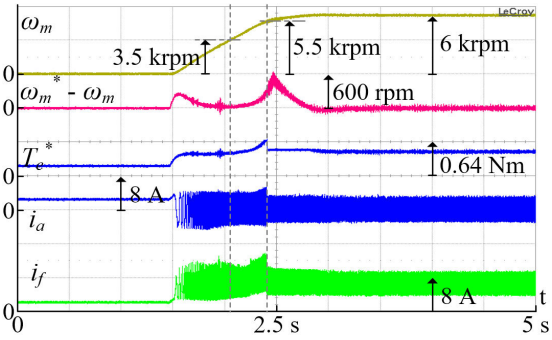

FIGURE 28. Responses when the machine accelerated from standstill to 6000 rpm within 1.25 s under 35% load.

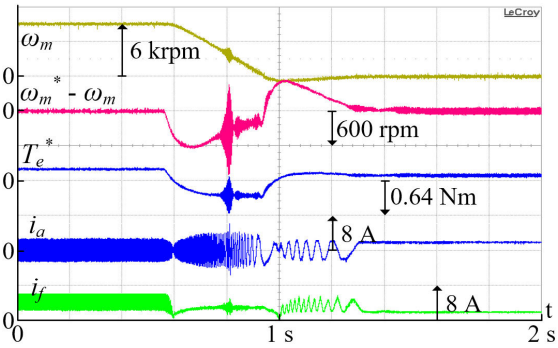

FIGURE 29. Responses when the machine decelerated from 6000 rpm to standstill under 25% load.

generation capability of the machine decreased as the speed increases. In addition, above 5500 rpm, the torque command was limited to 75% rated torque to maintain the stability of the speed control. The maximum speed error was approximately 600 rpm. The aforementioned results indicate that the designed control system can start the machine from standstill successfully and stably regulate the motor speed during acceleration and in the constant speed regions. Moreover, the speed response was smooth because of the small torque ripple.

Fig. 29 displays the responses when the machine decelerated from 6000 rpm to standstill under 25% load. Although the control system was stable, significant speed error was observed because the machine generated a large torque ripple due to the negative torque command.

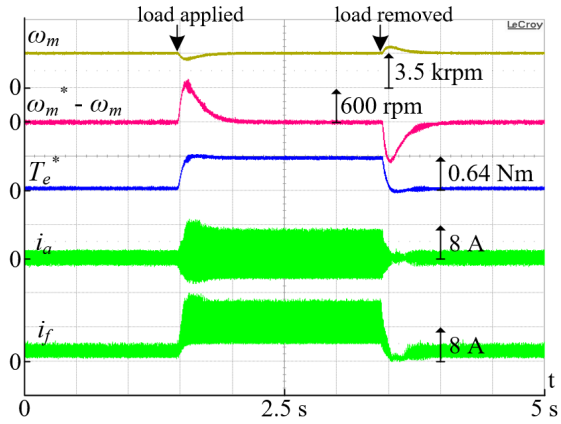

FIGURE 30. Responses when the machine ran at the rated speed and a step load of 90% rated torque was applied and removed.

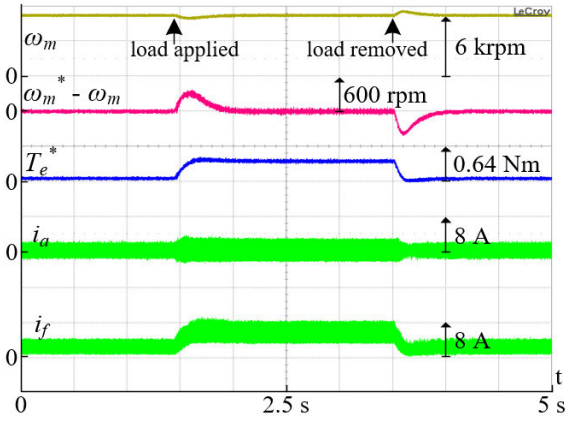

FIGURE 31. Responses when the machine was running at the maximum speed and a step load of 40% rated torque was applied and removed.

Figs. 30–32 illustrate the load rejection performance of the DCFSM control system. Fig. 30 displays the load rejection performance when the machine was running at 3500 rpm and a step load of 90% rated torque was applied. The controller required approximately 500 ms to control the shaft speed to the shaft speed command. The maximum speed error was approximately 669 rpm. After the load torque was removed, the shaft speed was controlled to the shaft speed command within 550 ms, and the maximum speed error was approximately 683 rpm. Fig. 31 depicts the load rejection performance when the machine was running at 6000 rpm and a step load of 40% rated torque was applied. The controller required approximately 450 ms to control the shaft speed to the shaft speed command, and the maximum speed error was approximately 215 rpm. After the load torque was removed, the shaft speed was controlled to the shaft speed command within 500 ms, and the maximum speed error was approximately 369 rpm. Fig. 32 displays the load rejection performance when the machine was running at 1750 rpm and a step load of −63% rated torque was applied. Because the torque ripple was large when producing negative torque, the speed error increased with the load. However, the speed controller could still successfully control the shaft speed to

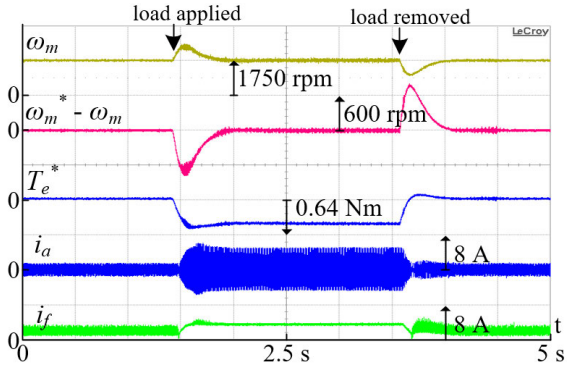

FIGURE 32. Responses when the machine was running at half the rated speed and a step load of −63% rated torque was applied and removed.

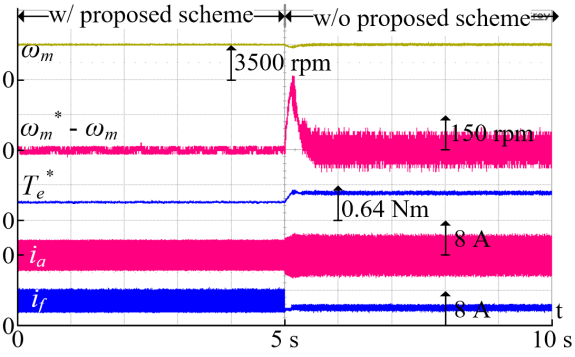

FIGURE 33. Responses when the machine was running at the rated speed with 50% load, the torque ripple reduction control was disabled at 5 s.

the shaft speed command after the load was applied and removed.

The results illustrated in Figs. 30–32 indicate that the control system designed for the single-phase DCFSM exhibits good speed regulation performance even under step load change.

Fig. 33 compares the responses with and without the proposed torque ripple reduction scheme. The machine was running at 3500 rpm with 50% rated load. The torque ripple reduction control was disabled at 5 s; then, the field current was control at 2.8 A, which is the minimum of the field current profiled for 50% rated torque. As it can be seen, large speed ripple occurred due to the significant torque ripple. The result illustrated that the proposed torque ripple reduction scheme can reduce torque ripple effectively.

The efficiency of the machine drive was also measured to further access the performance of the studied machine. The input power is the sum of the average power dissipated in the armature winding (P_a) and the field winding (P_f), which is shown by

$$P_{in} = P_a + P_f \tag{17}$$

where

$$P_a = \frac{1}{T}\int_0^T (v_a \cdot i_a)dt \tag{18}$$

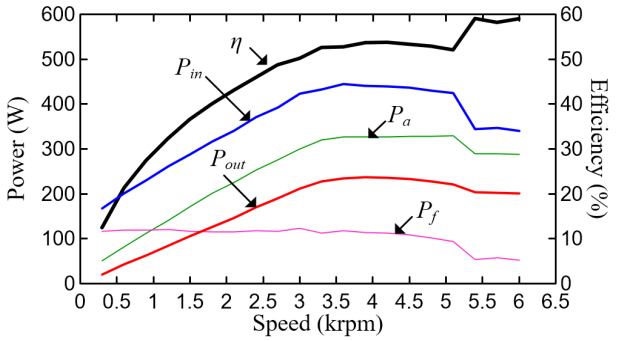

FIGURE 34. Measured power and efficiency versus speed as the DCFSM operate at the maximum torque condition.

$$P_f = \frac{1}{T}\int_0^T (v_f \cdot i_f)dt \tag{19}$$

where T denotes the integration period. The PWM ripple on the winding voltages was filtered carefully to avoid measurement error. The efficiency is calculated as

$$\eta = \frac{P_{out}}{P_{in}} \times 100\% \tag{20}$$

where

$$P_{out} = \omega_m \cdot T_e \tag{21}$$

Figure 34 illustrates the measured efficiency at the maximum torque conditions shown in Fig. 23, which means that the machine operated along the magenta line before 5400 rpm, otherwise operated along the green line. It can be seen that the armature power increases with speed, but the field power is approximately constant. The efficiency of the machine is approximately 53% at the rated speed. After 5400 rpm, because the torque command is limited to 75% rated torque, the efficiency increased to 59 % at the maximum speed.

VI. CONCLUSION

This paper presents a novel control scheme for single-phase DCFSMs. In this scheme, the machine is excited with current profiles that use the reluctance torque generated by the field current to compensate for the electromagnetic torque pulsations. Therefore, the torque ripple can be reduced considerably. The torque ripple is generally above 100% when the conventional control scheme is adopted; however, the torque ripple is less than 56% when the proposed control scheme is employed. The experimental results indicate that the proposed control system exhibits satisfactory speed regulation performance in DCFSMs due to its highly linear torque response. With the proposed control system, DCFSMs can robustly start from standstill under load and accelerate to the rated or maximum speed. Moreover, the proposed control system can effectively recover from a step load change in less than 0.5 s when the DCFSM runs at a constant speed.

The efficiency of the studied single-phase DCFSM motor drive is between 53–59%. This is comparable to the efficiency of commercially available single-phase IMs and UMs. However, with the proposed control scheme, the studied machine performs significantly better in speed regulation and torque ripple reduction. Consequently, it is possible to use the proposed single-phase DCFSM in the applications in which single-phase IM or UM is adopted.

REFERENCES

[1] Y.-J. Zhou and Z.-Q. Zhu, "Comparison of low-cost single-phase wound-field switched-flux machines," *IEEE Trans. Ind. Appl.*, vol. 50, no. 5, pp. 345–3335, Sep./Oct. 2014, doi: 10.1109/TIA.2014.2311511.

[2] Y. Tang, J. J. H. Paulides, and E. A. Lomonova, "Energy conversion in DC excited flux-switching machines," *IEEE Trans. Magn.*, vol. 50, no. 11, pp. 1–4, Nov. 2014, doi: 10.1109/TMAG.2014.2325405.

[3] Z.-C. You, S.-M. Yang, C.-W. Yu, Y.-H. Lee, and S.-C. Yang, "Design of a high starting torque single-phase DC-excited flux switching machine," *IEEE Trans. Ind. Electron.*, vol. 64, no. 12, pp. 9905–9913, Dec. 2017, doi: 10.1109/TIE.2017.2696486.

[4] C. Pollock, H. Pollock, and M. Brackley, "Electronically controlled flux switching motors: A comparison with an induction motor driving an axial fan," in *Proc. 29th Annu. Conf. IEEE Ind. Electron. Soc. (IECON)*, Roanoke, VA, USA, Nov. 2003, pp. 2465–2470, doi: 10.1109/IECON.2003.1280632.

[5] H. Pollock, C. Pollock, R. T. Walter, and B. V. Gorti, "Low cost, high power density, flux switching machines and drives for power tools," in *Proc. 38th Annu. Meeting Conf. Rec. Ind. Appl. Conf. (IAS)*, Salt Lake City, UT, USA, 2003, pp. 1451–1457, doi: 10.1109/IAS.2003.1257748.

[6] C. Pollock, H. Pollock, R. Barron, J. R. Coles, D. Moule, A. Court, and R. Sutton, "Flux-switching motors for automotive applications," *IEEE Trans. Ind. Appl.*, vol. 42, no. 5, pp. 1177–1184, Sep. 2006, doi: 10.1109/TIA.2006.880842.

[7] J. F. Bangura, "Design of high-power density and relatively high-efficiency flux-switching motor," *IEEE Trans. Energy Convers.*, vol. 21, no. 2, pp. 416–425, Jun. 2006, doi: 10.1109/TEC.2006.874243.

[8] Y. Chen, S. Chen, Z. Q. Zhu, D. Howe, and Y. Y. Ye, "Starting torque of single-phase flux-switching permanent magnet motors," *IEEE Trans. Magn.*, vol. 42, no. 10, pp. 3416–3418, Oct. 2006, doi: 10.1109/TMAG.2006.879437.

[9] L. I. Iepure, L. Tutelea, and I. Boldea, "FEM analysis and control of a tapered airgap single phase PMSM," in *Proc. 11th Int. Conf. Optim. Electr. Electron. Equip.*, Brasov, Romania, May 2008, pp. 241–248, doi: 10.1109/OPTIM.2008.4602373.

[10] C.-L. Chiu, Y.-T. Chen, and W.-S. Jhang, "Properties of cogging torque, starting torque, and electrical circuits for the single-phase brushless DC motor," *IEEE Trans. Magn.*, vol. 44, no. 10, pp. 2317–2323, Oct. 2008, doi: 10.1109/TMAG.2008.2000761.

[11] M. Fazil and K. R. Rajagopal, "A novel air-gap profile of single-phase permanent-magnet brushless DC motor for starting torque improvement and cogging torque reduction," *IEEE Trans. Magn.*, vol. 46, no. 11, pp. 3928–3932, Nov. 2010, doi: 10.1109/TMAG.2010.2057514.

[12] A.-S. Isfanuti, L. N. Tutelea, I. Boldea, and T. Staudt, "Small-power 4 stator-pole stator-ferrite PMSM single-phase self-starting motor drive: FEM-based optimal design and controlled dynamics," in *Proc. Int. Conf. Optim. Electr. Electron. Equip. (OPTIM) Int. Aegean Conf. Electr. Mach. Power Electron. (ACEMP)*, Brasov, Romania, May 2017, pp. 517–522, doi: 10.1109/OPTIM.2017.7975020.

[13] A. Mora, A. Orellana, J. Juliet, and R. Cardenas, "Model predictive torque control for torque ripple compensation in variable-speed PMSMs," *IEEE Trans. Ind. Electron.*, vol. 63, no. 7, pp. 4584–4592, Jul. 2016, doi: 10.1109/TIE.2016.2536586.

[14] Q. Fei, Y. Deng, H. Li, J. Liu, and M. Shao, "Speed ripple minimization of permanent magnet synchronous motor based on model predictive and iterative learning controls," *IEEE Access*, vol. 7, pp. 31791–31800, 2019, doi: 10.1109/ACCESS.2019.2902888.

[15] K. Xia, Y. Ye, J. Ni, Y. Wang, and P. Xu, "Model predictive control method of torque ripple reduction for BLDC motor," *IEEE Trans. Magn.*, vol. 56, no. 1, pp. 1–6, Jan. 2020.

[16] A. Abbaszadeh, D. Arab Khaburi, and J. Rodríguez, "Predictive control of permanent magnet synchronous motor with non-sinusoidal flux distribution for torque ripple minimisation using the recursive least square identification method," *IET Electr. Power Appl.*, vol. 11, no. 5, pp. 847–856, May 2017, doi: 10.1049/iet-epa.2016.0315.

[17] L. Yan, Y. Liao, H. Lin, and J. Sun, "Torque ripple suppression of permanent magnet synchronous machines by minimal harmonic current injection," *IET Power Electron.*, vol. 12, no. 6, pp. 1368–1375, May 2019, doi: 10.1049/iet-pel.2018.5647.
[18] J. Faiz, M. Heidari, and H. Sharafi, "Torque ripple and switching frequency reduction of interior permanent magnet brushless direct current motors using a novel control technique," *IET Power Electron.*, vol. 12, no. 14, pp. 3852–3858, Nov. 2019, doi: 10.1049/iet-pel.2018.6303.
[19] G. J. Li, K. Zhang, Z. Q. Zhu, and G. W. Jewell, "Comparative studies of torque performance improvement for different doubly salient synchronous reluctance machines by current harmonic injection," *IEEE Trans. Energy Convers.*, vol. 34, no. 2, pp. 1094–1104, Jun. 2019, doi: 10.1109/TEC.2018.2870753.
[20] Z.-C. You and S.-M. Yang, "Modeling torque characteristic of single-phase DC-excited flux switcing motor for torque ripple reduction," in *Proc. 44th Annu. Conf. IEEE Ind. Electron. Soc. (IECON)*, Washington, DC, USA, Oct. 2018, pp. 565–570, doi: 10.1109/IECON.2018.8591476.
[21] H. Hou, W. Yao, and W. Zhang, "Vector control of single phase brushless DC motor," in *Proc. 19th Int. Conf. Elec. Mach. Syst. (ICEMS)*, Chiba, Japan, 2016, pp. 1–5.
[22] M. Jemli, H. B. Azza, M. Boussak, and M. Gossa, "Sensorless indirect stator field orientation speed control for single-phase induction motor drive," *IEEE Trans. Power Electron.*, vol. 24, no. 6, pp. 1618–1627, Jun. 2009, doi: 10.1109/TPEL.2009.2014867.
[23] M. B. de Rossiter Correa, C. B. Jacobina, A. M. N. Lima, and E. R. C. da Silva, "Rotor-flux-oriented control of a single-phase induction motor drive," *IEEE Trans. Ind. Electron.*, vol. 47, no. 4, pp. 832–841, Aug. 2000, doi: 10.1109/41.857963.
[24] D.-H. Jang, "Problems incurred in a vector-controlled single-phase induction motor, and a proposal for a vector-controlled two-phase induction motor as a replacement," *IEEE Trans. Power Electron.*, vol. 28, no. 1, pp. 526–536, Jan. 2013, doi: 10.1109/TPEL.2012.2199772.
[25] S. Walz, R. Lazar, G. Buticchi, and M. Liserre, "Dahlin-based fast and robust current control of a PMSM in case of low carrier ratio," *IEEE Access*, vol. 7, pp. 102199–102208, 2019, doi: 10.1109/ACCESS.2019.2927402.

ZIH-CING YOU was born in Taiwan. He received the M.S. degree in electrical engineering from the National Taipei University of Technology, Taipei, Taiwan, in 2017, where he is currently pursuing the Ph.D. degree. His research interests include ac motor drive and control.

SHENG-MING YANG (Member, IEEE) was born in Taiwan. He received the M.S. and Ph.D. degrees from the University of Wisconsin-Madison, in 1985 and 1989, respectively. From 1989 to 1992, he was a Development Engineer with Unico Inc., and from 1992 to 1995, he was a Principal Engineer with the Corporate Technology Center, A. O. Smith Company, Milwaukee, Wisconsin. In 1995, he joined Tamkang University, Taiwan, as a Professor with the Department of Mechanical and Electro-Mechanical Engineering. Since 2007, he joined the Department of Electrical Engineering, National Taipei University of Technology, Taiwan. His research interests are ac and dc motor drives and control.